DESIGN AND DRAG REDUCTION PERFORMANCE ANALYSIS OF A POTATO HARVEST SHOVEL BASED ON THE SURFACE TEXTURE CHARACTERISTICS OF PANGOLIN SCALE
/
基于穿山甲鳞片表面纹理特征的马铃薯挖掘铲设计及减阻性能分析

Ping ZHAO*), Tiankuo YU, Guofa XU, Ruijin GUO, He LI, Hongfei XU, Tianci JIN, Dong JI
College of Engineering, Shenyang Agricultural University, Shenyang 110866 / China
Tel: +86-13591675814.; E-mail: zhaopingxdg@163.com

ABSTRACT
Taking into account the physicochemical properties of soil and the complexity of adhesion interface, how to improve the soil adhesion on the mechanical surface is a crucial technical issue. In order to lower the increasing resistance caused by soil adhesion on the surface of a digging shovel in potato harvesting, a potato digging shovel with a non-smooth surface structure was designed based on bionics theory. Based on testing physical and mechanical properties of soil, a soil groove model corresponding to soil physical properties and particle model physical properties was established through a combination of simulation and physical tests, and a simulation test for evaluating the drag reduction performance was conducted. The simulation comparison test results show that the performance of the bionic digging shovel is better than that of the traditional potato digging shovel, regardless of whether the broken soil rate or the working resistance is reduced, and the soil adhered to the mechanical surface can be effectively reduced by 93.3%. The research results can provide ideas and methods for solving the adhesion problem between machinery and soil.

摘要
考虑到土壤的理化性质和粘附表面的复杂特性，如何改善土壤与机具表面之间的粘附状况是一个非常重要的技术问题。为解决马铃薯收获过程中因土壤粘附于挖掘铲表面造成阻力增大的问题，基于仿生学理论设计了一种具有非光滑表面结构的马铃薯挖掘铲。在测得土壤表征参数的基础上，通过仿真与物理试验相结合的方法，建立了与土壤物理特性和颗粒模型物理特性相对应的土槽模型，通过模拟仿真对减阻效果进行了评估。通过对比仿真与试验，结果表明，无论碎土率还是工作阻力，仿生挖掘铲的效果都优于传统的马铃薯挖掘铲，且土壤和粘附在机械表面的数量可以有效地降低 93.3%。该研究结果可以为解决机具与土壤的粘附问题提供思路和方法。

INTRODUCTION

Potatoes are an important global non-grain food crop, industrial raw material, and feed crop *(Celik et al., 2019)*. In 2018, the total planting area of potatoes worldwide was 1.8×10^7 hm², with a total yield of 3.7×10^8 t. China accounts for approximately 27% of all potato planting areas, producing 24% of the total global output, ranking first worldwide *(Tong et al., 2000)*. The planting area of potatoes increases every year as potatoes are the fourth most important food crop in China. Therefore, potato-harvesting machinery has become an urgent necessity in the current Chinese market.

The harvesting shovel, which is utilised in the first step of harvesting operations and is an indispensable part of the potato harvester, is used for soil entry and excavation. Because China's planting area's geographical and soil problems are relatively dispersed, some mountainous and hilly areas have a high planting area, which determines the production mode for harvesting, transportation, and manual labour for picking and separation. The common problems associated with potato harvesting include separating clay from potatoes, potato skin rubbing from sandy soil, and increased back soil resistance. Scholars from various countries who are improving potato harvesting machinery have proposed innovative research and achieved beneficial results *(Babbitt, 2008; Hou et al., 2020)*. Although this lays a foundation for further research, soil adhesion on the shovel surface is gradually changed from mechanical contact to soil-to-soil contact (Fig. 1), energy consumption, specifically in some areas where the soil is relatively humid. Additionally, the soil interface adhesion system's overall mechanical behaviour is more severe during operation *(Zenkov, et al., 2020; Jafar et al., 2021)*.
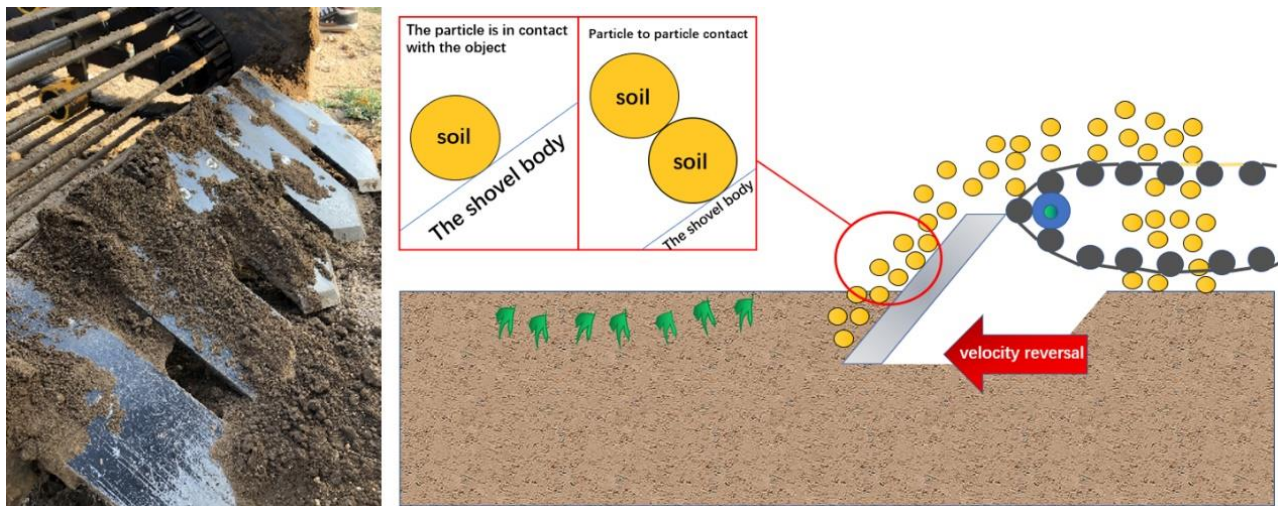
Fig. 1 - Soil stickiness

Therefore, a single force or analytical formula cannot solve the complex soil adhesion problem. There is no accurate and reasonable theoretical basis for the design and research of excavation components, as it is still in the empirical design stage.

In recent years, with the introduction of the advanced concept of bionics by industry peers extensively applying bionic technology and reverse technology in the engineering field *(Junior et al., 2019)*, simulation technologies have proven to be able to solve the problem of insufficient experience in the design of mechanical parts *(Wang et al., 2020)*, such as folding wings of bamboo elephants *(Tong et al., 2015)* and a chicken-like corn seed threshing machine *(Arnell et al., 2007)*.

After several million years of evolutionary optimization, many soil animals move freely in soil or manure without adhering to the outside, such as the armoured pangolin, mole crickets, ants, and moulting. This mobility feature is undoubtedly related to their peculiar body surface morphology. The corrugated surface model analysis shows that a corrugated surface can effectively reduce the soil adhesion area, reduce the negative air pressure at the interface, limit the continuity of the water film, and improve the lubrication of the interface and reduce the viscosity and resistance *(Massah et al.,2020)*.

After years of research, Jilin University in China has divided common geometric shapes into prismatic, concave, convex hull, flake, and spiral *(Zhang et al., 2004)*. The results show that a non-smooth surface has a certain effect on clay reduction and de-soiling *(Ren, et al.,2001; Liu et al.,2016; Junio et al.,2019)*, whereas a ridge structure is relatively easy to control. The pangolin is often found in the humid forest areas of hills, foothills, and plains. Because the pangolin can dig 20~30 cm diameter holes 2~4 m deep in the soil, it is the source of bionic ridge structure. When pangolins use their claws to dig holes through the mountain nail quickly, the pangolin body's scale resists the loosened soil, causing the soil to be pushed out of the hole *(Lee et al., 2001)*. The scale surface on pangolins shows a non-equiangular geometric mesh shape with crisscross changes of longitudinal ridges and transverse grooves. The longitudinal ridges are more prominent and more numerous, with a fan-shaped distribution. The transverse grooves are small and less numerous, and the longitudinal ridge is cut at a certain depth *(Lee et al., 2001; Zhou et al., 2016)*. This biological prototype for a soil removal tool exhibits a satisfactory drag reduction, and its working environment or soil flow on the surface is close to the working condition of the harvesting shovel.

At the same time, it was observed that the scales of pangolins were about 22.5°, while the optimal entry angle of potato harvest shovel was about 24° (Fig. 2).

Combined with the soil digging behaviour of pangolins, the scales would be slightly adjusted with the body surface muscle, so it was thought that they had a lot in common.

This study investigates the attachment of a ridge structure to the potato harvest shovel to reduce viscosity and add a de-soiling to reduce soil adhesion on the shovel surface and minimise resistance to back soil function. This study also provides both mode and method for addressing surface mechanical viscosity reduction and de-soiling that is yet to be solved entirely.
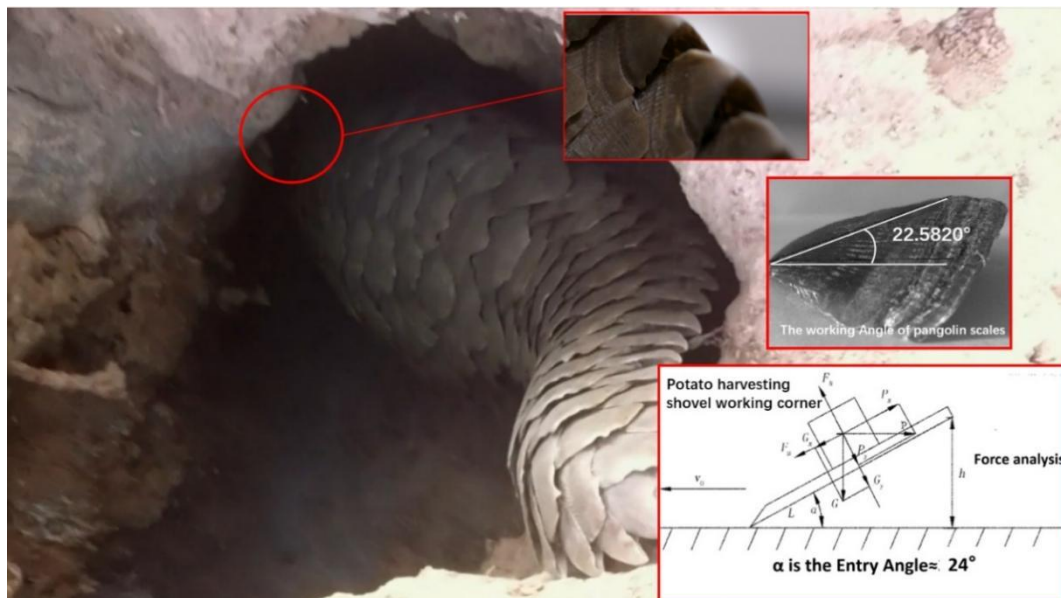
**Fig. 2 - Comparison diagram of soil digging behaviour of pangolin and
the design of soil digging angle of potato harvesting shovel**

MATERIALS AND METHODS
Point cloud data pre-processing and structure feature extraction of target samples
Point cloud data acquisition and processing of squamous perforator

To understand the distribution of ridges on the surface of scales, information on ridge structure characteristics was obtained using reverse engineering technology. Since pangolins are world class protected animals and require research authorization, the choice in this case was to study rare pangolin specimens with the assistance of Shenyang Museum of Natural History, China. The natural death scale of Chinese pangolin *(Heath et al.,1986)* was used as the test material. Before the experiment, the surface of the material was cleaned using 50% alcohol. The ridge spacing was confirmed after observing the surface structure using an ultra-depth scanning electron microscope. To avoid distortion and reflection due to other factors, such as environmental light, an FC-5 contrast enhancer was sprayed on the material's surface while scanning *(Xu et al., 2020).* After spraying, the data points on the surface of the scale were collected using a three-dimensional scanner VTOP 200 T. Based on pre-processing, such as point cloud multi-view stitching and denoising *(Hao et al., 2021)*, the scale model of the armour was reconstructed by reverse engineering technology, and the error was controlled within the allowable error range of ±5% *(Liu et al.,2016; Hu, 2015)* to ensure the validity of the model. The overall process is as follows (Fig. 3).
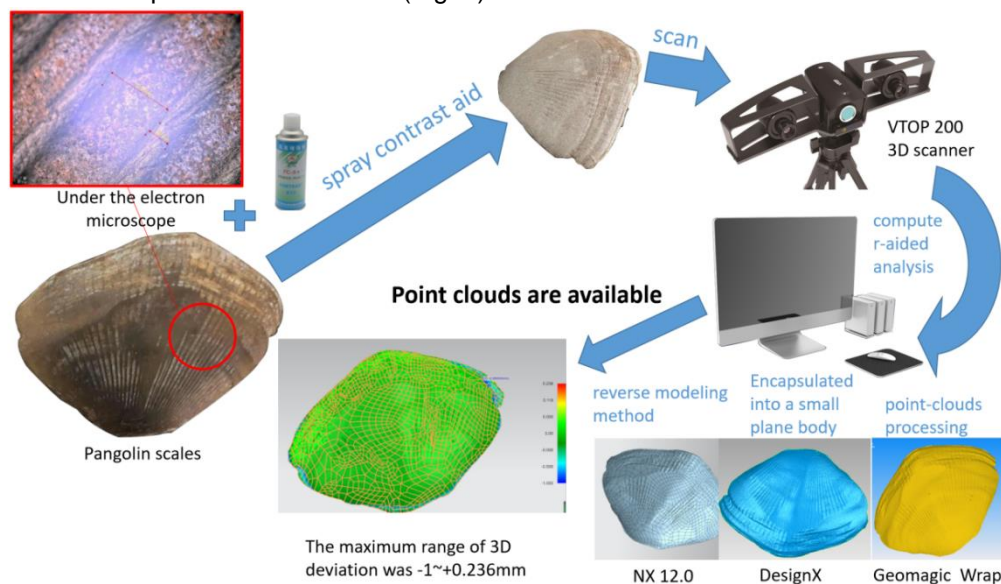

Fig. 3 - Process of point cloud acquisition and checking

Extraction of pangolin scale surface structure characteristics

As bioinspiration should not rely on the mere copying of nature *(Greiner et al., 2015)*. According to the observation, it is impossible to judge which function rule is consistent with the outer contour of pangolin scales, so polynomial fitting method is adopted to fit it. Based on the Curve Fitting function in the Toolboxes directory of MATLAB, surface Fitting (CF Tool) was selected to perform polynomial Fitting on the point cloud data.

Ridge line:

The central ridge is to be extracted by setting a vertical plane through the scale point cloud using Geomagic Control, as shown in Fig. 4.
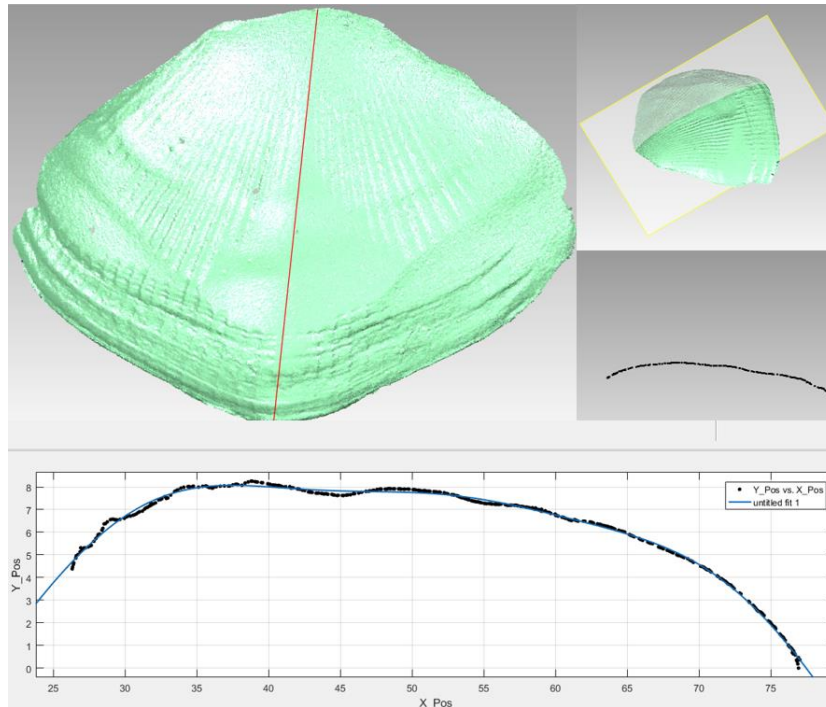
Fig. 4 - Extraction and fitting process of the outer ridge contour

Based on MATLAB, the point cloud data is fitted and its equation is obtained as follows:

$$f(x) = -1.442 \times 10^{-8} x^6 + 4.557 \times 10^{-6} x^5 + 6.02 \times 10^{-4} x^4 + 0.04197 x^3 - 1.635 x^2 + 33.75x - 280.7 \quad (1)$$

As shown in Table 1, with the exponential of x increasing, the values of SSE and $RMSE$ of MATLAB polynomial surface fitting for the three-dimensional coordinate data of the point cloud are decreasing and the coefficient of determination (R^2) is increasing, indicating that the fitting surface is closer to the actual pangolin surface contour with the exponential increase of x. However, when the index of x increases to 4, the values of SSE, $RMSE$ and R^2 change little for each index of independent variable. For example, when the index of x increases from x^4 to x^5, the square of residual (SSE) decreases from 8.639 to 7.92, and the mean square error ($RMSE$) decreases from 0.1481 to 0.142. The coefficient of determination increased from 0.9947 to 0.9952. For example, when the index of x increases from x^5 to x^6, the square of residual error (SSE) decreases from 7.92 to 5.395, the mean square error ($RMSE$) decreases from 0.1481 to 0.142, and the determination coefficient increases from 0.9952 to 0.9967. When the exponents are 8, the surface fitting result is SSE=4.682, $RMSE$=0.1096, R^2=0.9972, and the determination coefficient is close to 1. For the fitting result of complex biological surface, the fitting accuracy meets the fitting requirements. In summary, the power of x is 6.

Table 1

Fitting results of outer contour lines of different exponents

x^n	SSE	R^2	Adjusted R^2	$RMSE$
4	8.639	0.9948	0.9947	0.1481
5	7.920	0.9952	0.9952	0.1420
6	5.395	0.9967	0.9967	0.1173
7	4.952	0.9970	0.9970	0.1125
8	4.682	0.9972	0.9971	0.1096

Note: x^n means that the highest index of x was n. SSE is residual sum of squares, RMSE is mean square error, the same as below.

Rib texture

As the amount of point cloud data will affect the subsequent surface fitting, the point cloud model processed by the Geomagic Wrap was imported into the Geomagic Control and divided into nine areas for observation. The effective surfaces with clear structure B, C, D, E and F were selected as the research objects, and the rest areas were subdivided. Point cloud is a collection of scattered points in space, which represents the contour feature information of the object surface. Point cloud slices are intersected with point cloud by a group of planes. Through the function of cross section under the start menu, a section perpendicular to the surface was established and the number of external contour lines was exported, as shown in Fig. 5. After the export, the data points were roughly between 380 and 450. The TXT coordinates were exported from the interface dat. file, and the data could be viewed by Excel or MATLAB (Fig. 5).
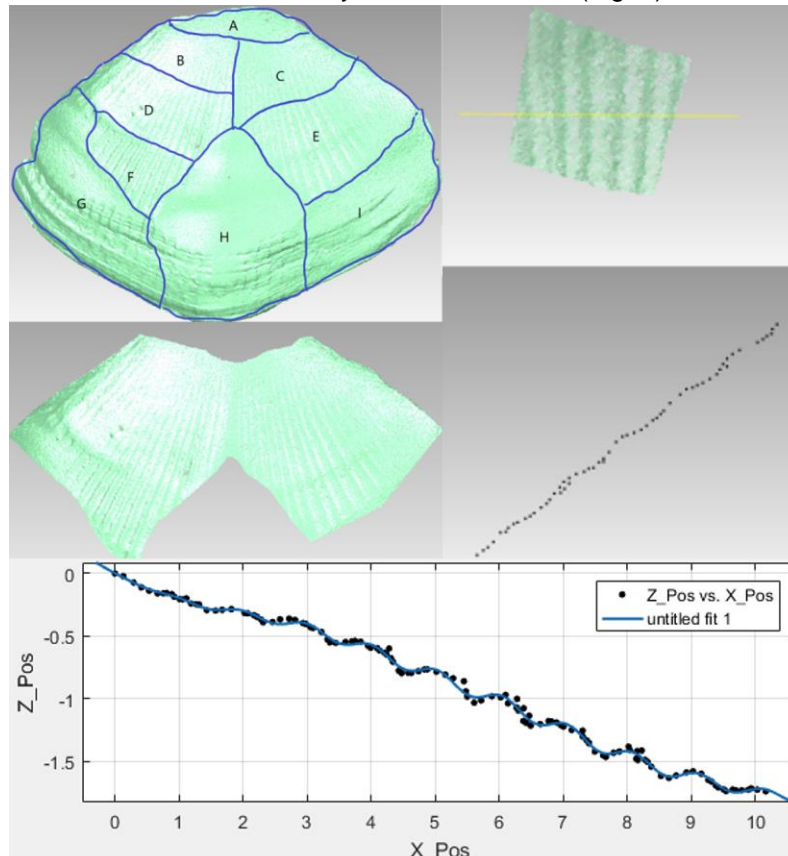
Fig. 5 - Derives the characteristic contour of the surface texture

The ridges on pangolin scales were observed to conform to some function law, so sinusoidal function fitting method was used to fit the ridges. Based on the Curve Fitting function in the Toolboxes directory of MATLAB, CF Tool was selected to perform sum of sin Fitting on the point cloud data. As shown in Table 2, with the exponential of x increasing, the values of SSE and $RMSE$ of MATLAB polynomial surface fitting of the three-dimensional coordinate data of the point cloud are continuously decreasing, and the coefficient of determination (R^2) is increasing. When the exponential of x is 6, it reaches the minimum, and then rises again. In this case, SSE and $RMSE$ are the minimum, R^2 is the maximum, and the determination coefficient is close to 1. As for the surface fitting results, the fitting accuracy meets the fitting requirements. In summary, the power of x is selected as 6, so the fitting equation of the surface texture of ribbed structure is as follows:

$$f(x) = 1.776\sin(0.2177x + 2.92) + 0.5651\sin(0.4075 - 0.7116) + 0.03001\sin(1.232x - 3.094)$$
$$+ 0.02179\sin(1.599x - 2.344) + 0.02896\sin(5.92 - 2.713) + 0.02541\sin(6.403x + 0.4)$$

(2)

Table 2

Fitting results of outer contour lines of different exponents

x^n	SSE	R^2	Adjusted R^2	$RMSE$
5	0.08247	0.9976	0.9973	0.02776
6	0.06915	0.9980	0.9976	0.02579
7	0.07028	0.9979	0.9975	0.02638

The expressions of ridges were obtained by function fitting, as shown below: the determination coefficient was approximately 1, and the fitting accuracy of the surface fitting results met the fitting requirements. Ridge line and the outer contour line of the surface rib texture jointly constitute the bionic surface, which provides the design basis for the subsequent bionic modeling.

Design and analysis of potato-digging shovel based on the ridge structure of the armoured pangolin

Design of bionic potato-harvesting shovel

The scale surface of a pangolin was observed, measured, and analysed under a super depth of field microscope (Fig. 6).
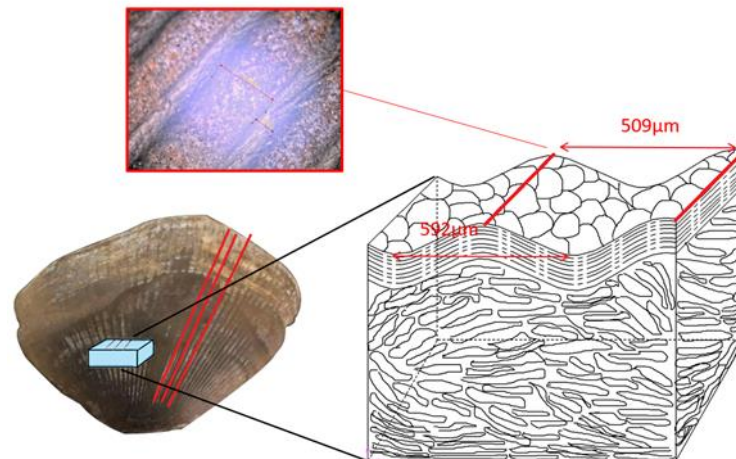

**Fig. 6 – The scale surface of pangolin was observed, measured and analysed
under a super depth of field microscope**

The distance between the two ribbons on the pangolin scales was measured at about 500 to 600 microns. Therefore, in the virtual modelling of rib arrangement, the rib structure was roughly divided into the following three categories (Fig. 7).
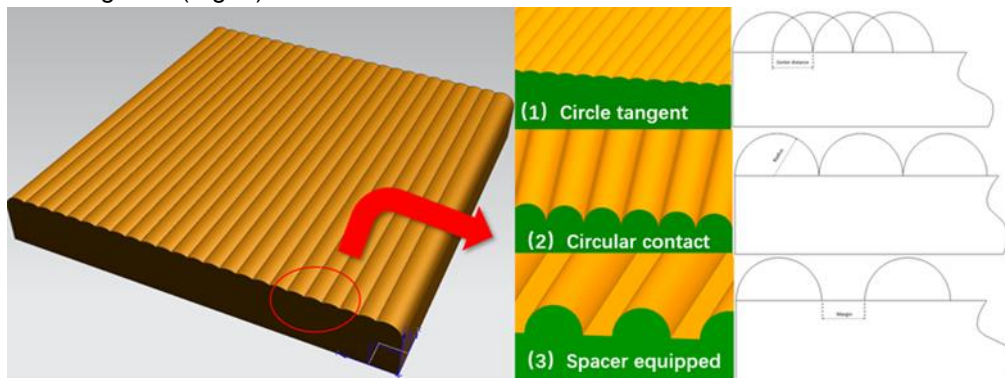

Fig. 7 – Three kinds of ribbed arrangement
(1)   Ribbed with tangential boundaries; (2) A closely arranged ribbed structure; (3) Ribbed with certain gaps

Considering that the problem of adhesion is a process of many a little makes a mickle, all the particles in the 15×15 mm soil tank used in the adhesion test were the smallest particles after screening, with radii of 0.3–0.5 mm. According to the above types, nine groups of ribbed surfaces with different radii and a smooth plane were established with dimensions of 10×10×1.5 mm. Based on the radii of 0.3, 0.4, and 0.5 mm, the ribbed edges with tangential edges were designated as C, those with dense edges were denoted as S, and those integrated into the ribbed edges with tangential edges were indicated by V. First, the experimental body was buried under the soil at an angle of 32.5°. In the filling process, the slope of the experimental body was 24°. When the soil particles were stable, the speed of the plane body was set, and the experimental body moved upward by 0.3 m/s. When most of the particles were clearly leaving the experimental surface, the motion of the experimental body was suspended. Inertia was used to remove the soil particles completely from the surface in the computing area. Then, the direction of gravity was reversed, the soil particles that were not attached to the plane body left the calculated area, and the results were compared. This approach reduced the CPU calculation load and accelerated the calculation process.

Fig. 8 depicts this procedure. (In EDEM, the gravity direction of soil particles can be reversed by modifying the gravity in the environment. Instead of dumping the soil by turning over the shovel, the soil left after the above operation is attached to the shovel surface. This method can quickly determine how many soil particles are adhered to the surface of the shovel surface.)
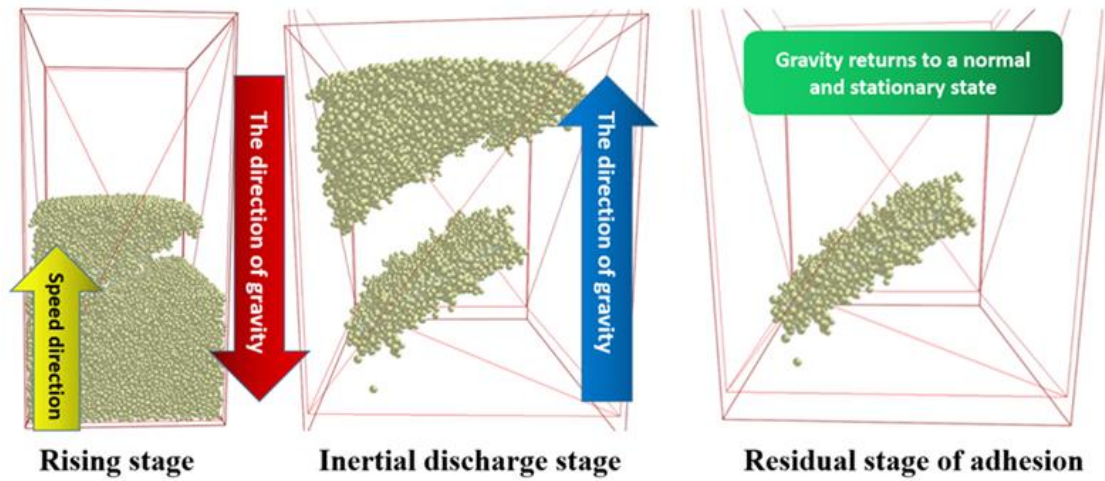

Fig. 8 – Three stages of soil particles

After comparing the simulation results (Fig. 9), it can be concluded that the surface residual soil values of the edge-cut type and the interval type with 0.5 mm radius are respectively 6.51×10^{-6} kg and 6.33×10^{-6} kg, which are less than those of other types.
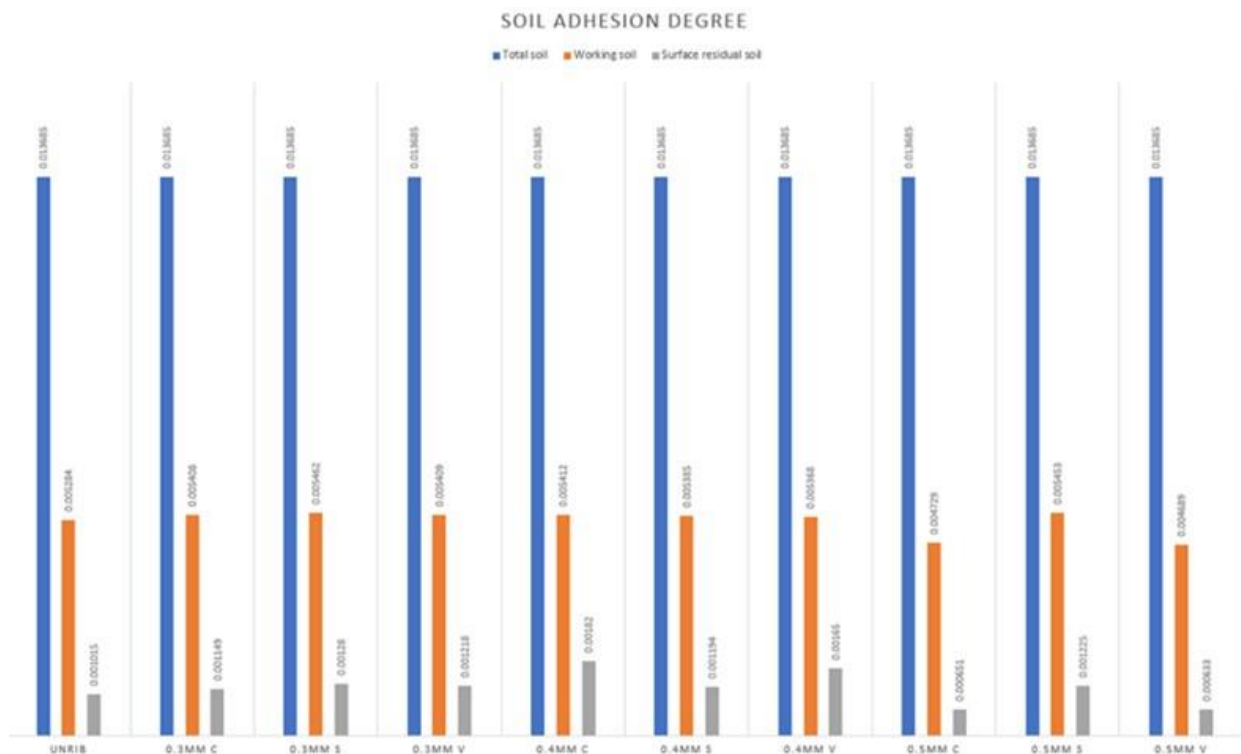

Fig. 9 – Comparison of soil residual conditions of 10 groups of different types of planar bodies

The seven types of potato-harvesting shovels presented in Fig.10 were designed based on the contour curve function obtained by the above software function. Each shovel was 10 mm thick, 335 mm long, and 131 mm wide. In addition to the enlarged ridge-type digging shovel, the ridge spacing of the non-smooth surface was 0.5 mm, and the ridge diameter was 0.5 mm. By establishing the above shovels with different overall shapes or surface smoothness, experimental subjects were provided for subsequent control experiments to explore the optimal arrangement of ribbed patterns.
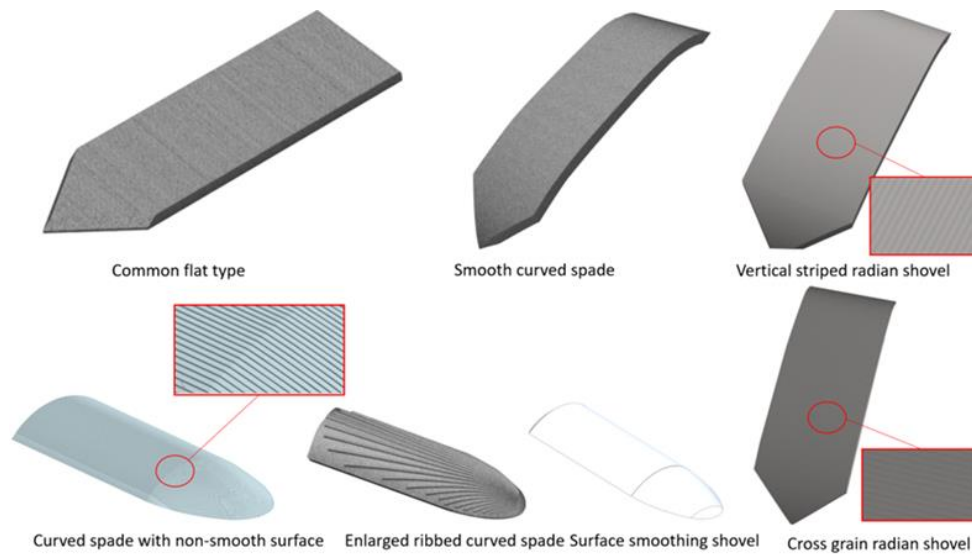
Fig. 10 – Types of shovels

Common flat type   Smooth curved spade   Vertical striped radian shovel

Curved spade with non-smooth surface   Enlarged ribbed curved spade   Surface smoothing shovel   Cross grain radian shovel

Simulation test analysis

Establishment of soil particle model:

The soil with a moisture content between 13% and 16% in Northeast China was used for simulation in this study. In capillary theory, soil adhesion is related to the interfacial water model tension *(Fisher, 1928)*.
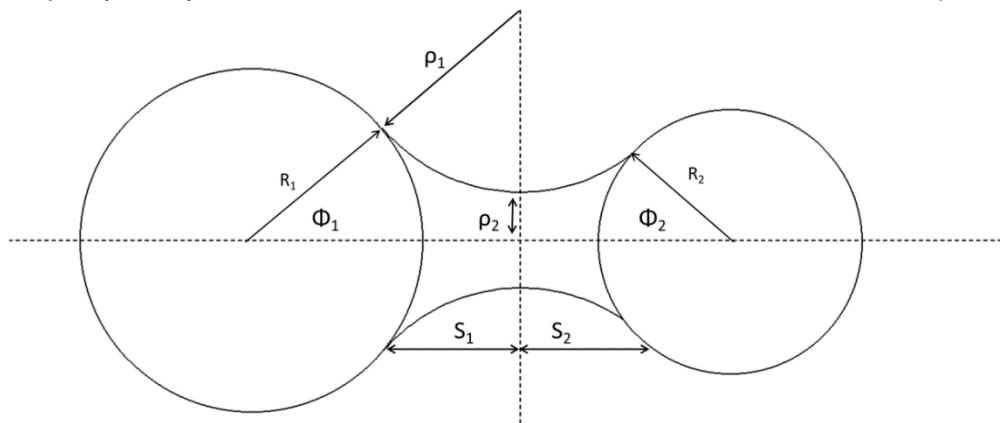

Fig. 11 - Water film tension model between two spherical soil particles

According to the Fisher theoretical model, as shown in Fig. 11, the water model tension, *P*, between two spherical particles is given by:

$$P = \pi r_2^2 \Delta\rho + 2\pi r_2 \gamma_{LV} \tag{3}$$

Under a certain moisture content, a water ring is formed to combine the particles, where ρ_1 and ρ_2 are the radii of the concave and convex surfaces, respectively; R_1 and R_2 are the radii of the particles; S_1 and S_2 are the distances from the particles to the liquid bridge neck; φ_1 and φ_2 are the wedge angles of the particles.

According to the study of Qiushanfeng and Hengjingzhao *(Yutaka et al., 1972)*, a solid intervention exists when the soil is divided into loose accumulation and dense accumulation. The model is transformed, as demonstrated in Fig. 12.
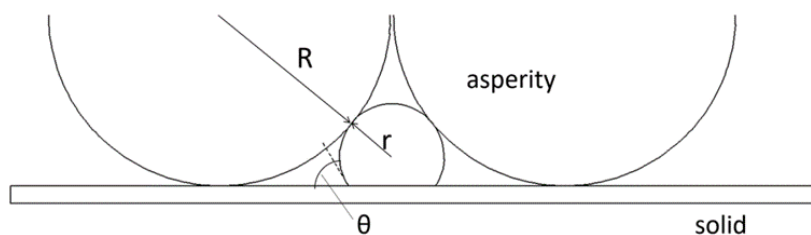

Fig. 12 - Schematic of the capillary channel between two soil particles and solid surface

The adhesion force, F_0, between soil particles and solid materials, which is a small-density accumulation of soil, can be expressed as follows:

$$F_0 = \frac{\pi(1+\cos\theta)\{(1+\cos\theta)(1+\cos\alpha) - \sin\alpha\}(\cos\theta + \cos\alpha)\gamma_{LV}}{4R}$$ (4)

The adhesion force between soil particles and solid materials, F_C, is given by

$$F_C = \frac{2}{\sqrt{3}}F_0$$ (5)

The adhesion force is primarily determined by the resultant force, F, of the following five forces:

$$F = F_m + F_e + F_c + F_b - F_p$$ (6)

Where F_m is the intermolecular attraction, F_e is the metal surface static attraction, F_c is the capillary force, F_b is the viscous resistance, F_p is the wedge resistance, and F_c plays a decisive role.

$$\gamma_{S/V} = \gamma_{S/L} + \gamma_{L/V}\cos\theta$$ (7)

According to the equation, $\gamma_{S/V}$ is the energy of the solid surface, $\gamma_{S/L}$ is the energy of solid/liquid interface, $\gamma_{L/V}$ is the energy of the liquid surface, and θ is the contact angle of the liquid droplet on the solid surface. Therefore, it was attempted to add the Johnson–Kendall–Roberts (JKR) model to the Hertz–Mindlin model to obtain the surface energy formula, expressed as follows:

$$F_{JKR} = -4\sqrt{\pi\gamma E^* \alpha^{3/2}} + \frac{4E^*}{3R^*}\alpha^3$$ (8)

$$\delta = \frac{\sqrt{4\pi\gamma\alpha}}{E^*} + \frac{\alpha^2}{R^*}$$ (9)

Where the contact spot radius, E^* and R^* are equivalent to Young's modulus and equivalent radius of the two spheres in contact, respectively, defined in terms of shear moduli of contacting spheres *(Baran et al., 2009)*.

$$F_{Hertz} = \frac{4}{3}E^*\sqrt{R^* * \sigma^{3/2}}$$ (10)

Before establishing a soil trough model, the contact parameters and contact model parameters must be calibrated according to the experimental site's intrinsic parameters, and the typical soil in Northeast China must be collected *(Hunt et al., 1984.* (Fig. 13).
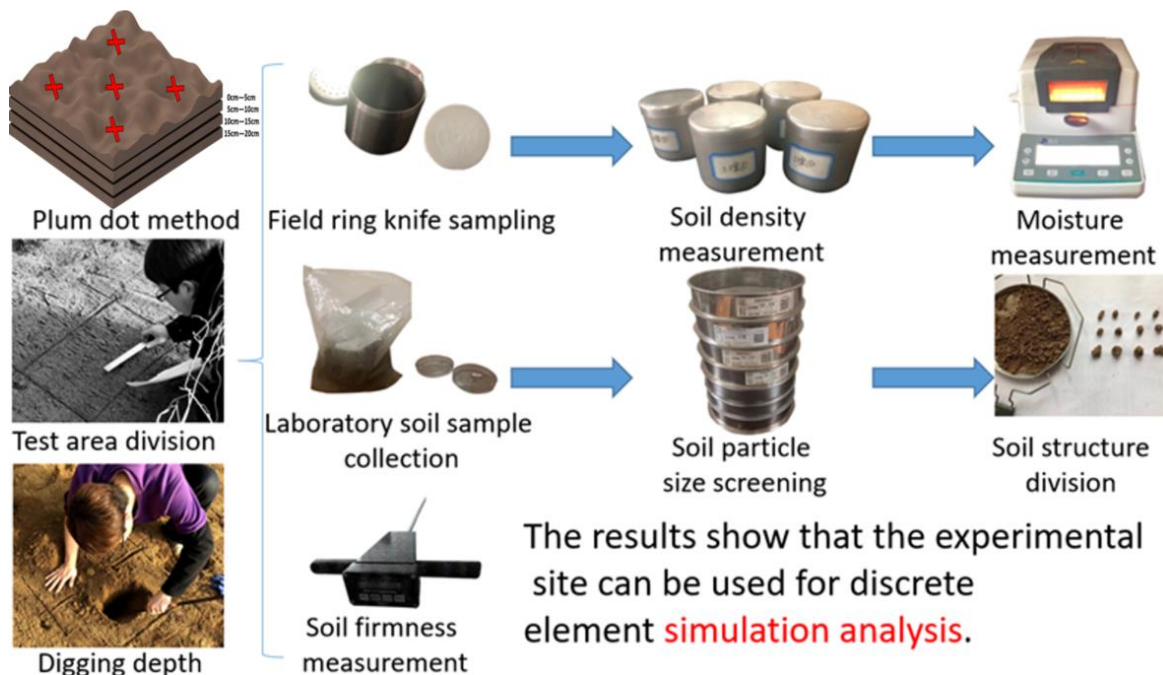

Fig. 13 - Determination of field soil intrinsic parameters

According to the above test steps, the experimental data in the following table can be obtained, as shown in Table 3.

Result of soil moisture content

Sampling point/depth	0~5cm	5~10cm	10~15cm	15~20cm
1	15.24%	14.79%	13.41%	14.92%
2	15.68%	15.56%	15.98%	15.75%
3	16.09%	16.08%	14.39%	14.70%
4	15.88%	13.35%	15.66%	15.39%
5	14.46%	14.71%	15.10%	15.43%
Average value	15.47%	14.898%	14.908%	15.238%

The average water content of five samples at different depths was counted. Then it was concluded that the water content was similar between 0 and 20 cm, and there was no preliminary conjecture that the water content of 0~5 cm was significantly greater than that of 15~20 cm, and the soil water content was 15.13%. The direction of movement of water in soil depends on its water potential, as in equation 11:

$$\phi_T = \phi_M + \phi_O + \phi_G + \phi_P \tag{11}$$

That is, the total water potential φ_T is the sum of matrix potential φ_M, solute potential φ_O, gravitational potential φ_G and pressure potential φ_P. Considering that it is a rainy season, the similarity of current moisture content to normal phenomenon is not an error caused by improper operation in the experiment process. There is still a distance from the soil layer with obvious change of moisture content. The moisture content data can provide an important theoretical basis for the selection of contact model in the subsequent discrete element software simulation process.

The test soil in this experiment was obtained from the test field in Heishan County, Jinzhou City, Liaoning Province. The soil samples were collected at 05:00 h. As potatoes are planted at a depth of approximately 20 cm in the ploughing layer, and moisture content is similar from 0 cm to 20 cm, it was not necessary to obtain the samples from different depths. When obtaining the soil samples, the soil around the ring knife was first cut with a paring knife, then the ring knife filled with soil was removed. The excess soil at both ends of the ring knife was removed, and the soil outside the ring knife was wiped. Both ends of the ring knife were covered immediately to prevent the evaporation of the moisture contained in the soil, then weighed (accurate to 0.01 g) and recorded. In the same layer, an aluminium box was used to obtain samples for subsequent experimental research. The ring knife holder was placed on the ring knife of known weight, and the ring knife edge was pressed downward and vertically into the soil until the ring knife barrel was filled with samples. Attention was paid to applying a stable and consistent force while pressing the ring knife. According to the density formula, the mass of the ring cutter is m_0, the total mass of the ring cutter and the soil sample is m_1, and V is the volume of the ring cutter, which is 100 cm^3. The density calculation formula is as follows:

$$\rho = \frac{1000(m_1 - m_0)}{V} \tag{12}$$

The densities of soil samples at depths of 0~20 cm can be obtained according to the above steps. Table 4 shows the test data.

Result of soil density

Sampling location	Soil mass / g	Soil volume / cm^3	Soil density / kg/m^3
1	168.01	100	1680
2	146.51	100	1465
3	158.77	100	1588
4	142.10	100	1421
5	154.61	100	1546
Average value	154.00	100	1540

According to the data in Table 4, the soil density of the site is approximately 1540 kg/m^3. After screening, the average value was calculated. Particles with radii exceeding 2 mm account for ~14.975% of all the particles. Those with radii between 1 mm and 2 mm account for ~22.075%. Those with radii between 0.5 mm and 1 mm account for ~12.19%, and those with radii less than 0.5 mm account for ~57.45%. According to the particle angle of repose China National Standard, the measurement device was built vertically from a height of 10 mm to the desktop at 80 mm, and the average angle of repose was measured to be 38.5065°. After establishing the ground using EDEM software, the circular plane with a diameter of 10 mm was set as the particle factory, and the particle radius was divided into four intervals: 2~3, 1~2, 0.5~1, and 0.3~0.5 mm. Design-Expert was used to analyse the data. Table 5 presents the analysis of variance of the angle of repose.

Table 5

Analysis of variance table of the angle of repose Y$_1$

	Sum of		Mean	F	P-value
Source	Squares	df	Square	Value	Prob > F
Model	2832.55	14	202.32	13.35	< 0.0001***
A-rolling friction	457.57	1	457.57	30.19	< 0.0001***
B-particle density	132.77	1	132.77	8.76	0.0103**
C-surface energy density	1652.92	1	1652.92	109.05	< 0.0001***
D-Poisson's ratio	55.08	1	55.08	3.63	0.0773*
AB	43.22	1	43.22	2.85	0.1134
AC	67.06	1	67.06	4.42	0.054*
AD	12.03	1	12.03	0.79	0.388
BC	3.43	1	3.43	0.23	0.6415
BD	1.35	1	1.35	0.089	0.7697
CD	105.38	1	105.38	6.95	0.0195**
A2	29.84	1	29.84	1.97	0.1824
B2	0.019	1	0.019	1.25 e-03	0.9723
C2	13.3	1	13.3	0.88	0.3649
D2	0.35	1	0.35	0.023	0.8816
Residual	212.21	14	15.16	-	-
Lack of Fit	179.45	11	16.31	1.49	0.4117
Pure Error	32.76	3	10.92	-	-
Cor Total	3044.76	28	-	-	-

*** *indicates extremely significant (P < 0.01); ** indicates significant (0.01 < P < 0.05); * indicates significant (0.05 < P < 0.1).*

Table 5 shows that the experimental model is significant (P < 0.01). The surface energy density and rolling friction have extremely significant effects on the soil accumulation angle, whereas the particle density and interaction CD (surface energy density and Poisson's ratio) significantly affect the soil accumulation angle. The order of the influence of the various factors and interaction factors on the bulb loss rate is A, C, B, CD, AC, and D, and the regression equation between the index and various factors is:

$$StackingAngle = 19.04809 - 187.02557\alpha + 0.026875\beta + 36.4122\lambda + 11.1048\gamma - 5.13\lambda\gamma \qquad (13)$$

where λ is the surface energy density, γ is Poisson's ratio, α is rolling friction between soil particles, and β is soil particle density. The friction angle was calibrated to 38.5° by adjusting the surface energy density and rolling friction parameters, as shown in Fig. 14.

There are many methods for measuring the stacking angle, and the funnel falling device structure was chosen which is more accurate and convenient to control, so that it is more in line with China's national standards for measuring discrete materials. Finally, the surface energy between the material and the particles was found to be 36.5 J/m^2, and the surface energy between the particles was 1 J/m^2.
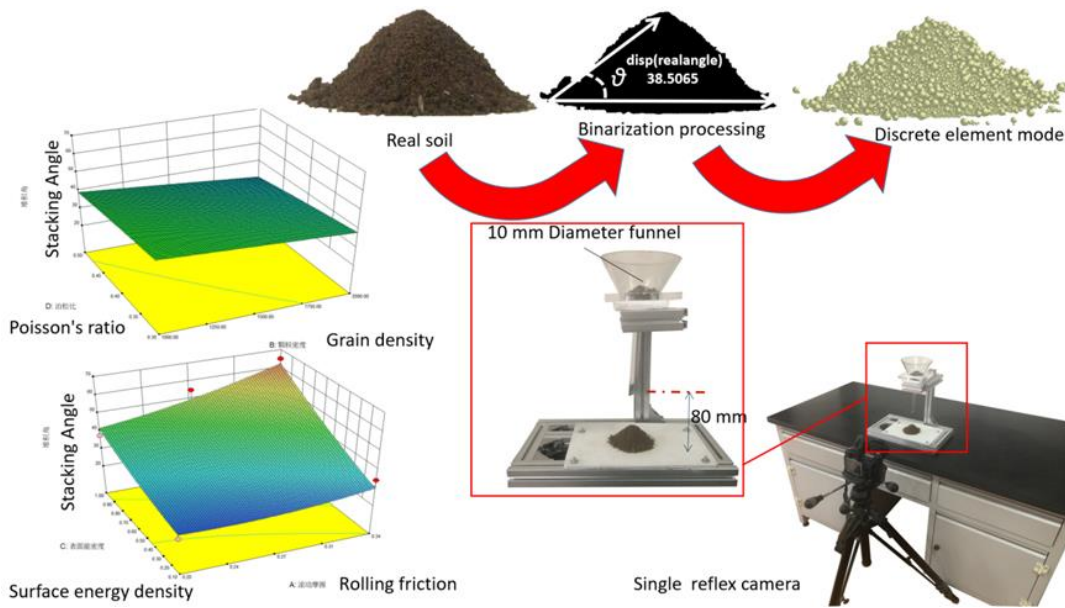
Fig. 14 - Parameter calibration experiment

Table 6 lists the other parameters. Based on these data, a realistic model of the target soil groove was built.

Table 6

EDEM parameter settings

Parameter	Unit	Numerical value
Poisson's ratio of soil particles	-	0.35
Shear modulus of soil particles	MPa	1.06
Density of soil particles	kg/m^3	1540
Poisson's ratio of 65 manganese	-	0.3
Shear modulus of 65 manganese	MPa	1.92
Density of 65 manganese	kg/m^3	7800
Recovery coefficient between particles	-	0.13
Rolling friction factor between particles	-	0.27
Static friction factor between particles	-	0.56
Recovery coefficient between particles and excavating shovel	-	0.16
Rolling friction factor between particles and excavating shovel	-	0.5
Static friction factor between particles and excavating shovel	-	0.43
Simulation time step	S	13.2
Acceleration of gravity	m/s^2	9.81

Establishment of test soil tank model

Owing to the complexity of the soil composition, it is challenging to explain the adhesion problems of machinery in soil disturbance using a single force. With the destruction of the stable soil structure, the total surface area of the particles increases, the surface energy becomes large, and the adhesion becomes severe. Therefore, to accelerate the calculation, a 400×350×330 mm calculation domain was established to move with the shovel and perform the dynamic auxiliary calculation. Soil entry is the initial state of the shovel body. With the accumulation of granular beds, the 350×243×500 mm soil grooves were elongated to 350×243×1200 mm after the granular bed particles were stabilized at 0.5001 s to simulate the actual soil environment. Subsequently, the amount of soil in the space was calculated when the soil grooves moved in the x-direction at a speed of 0.5 m/s, stopped at 4 s, moved in the z-direction at a speed of 0.5 m/s, and stopped at 5 s.

Fig.15 depicts the soil groove model. A completely closed soil groove will cause incorrect soil displacement. Therefore, the wall was dismantled in stages during the simulation process and designed a kind of soil groove model similar to a matchbox, and thus eliminated the rebound force of motion potential energy acting on the wall.
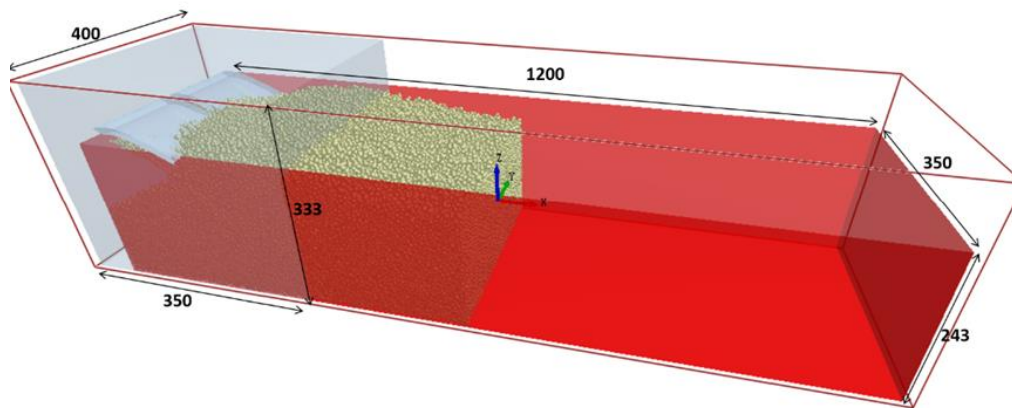

Fig. 15 - Modified soil model

RESULTS

Fig. 16 presents the results of the potato-harvesting simulation. The proposed harvesting shovel with a ridge-type non-smooth (HD) surface is clearly more effective than other harvesting shovels in reducing clay and soil. The soil removal effect directly affects the size of soil particles in the spatial grid of each shovel. After dividing the particles in the region in which the shovel was located, the soil volume attached to the conventional flat-type shovel (PB) surface is 312.9416 mm^3 per unit time after process termination. Compared with the flat type, the single-direction radian shovel designed by the ridge function has 295.693 mm of soil attached to it after process termination because of its unique angle. Therefore, the outer contour has a certain influence on soil removal. Simultaneously, it bends along the function of the pangolin scale from the front and back directions as well as the left and right, but the surface is relatively smooth and has no ridge structure (QG). After the work stops, the attached soil volume is 270.4352 mm^3, which is better than that in the single direction case, further confirming the influence of the outer contour on soil removal.
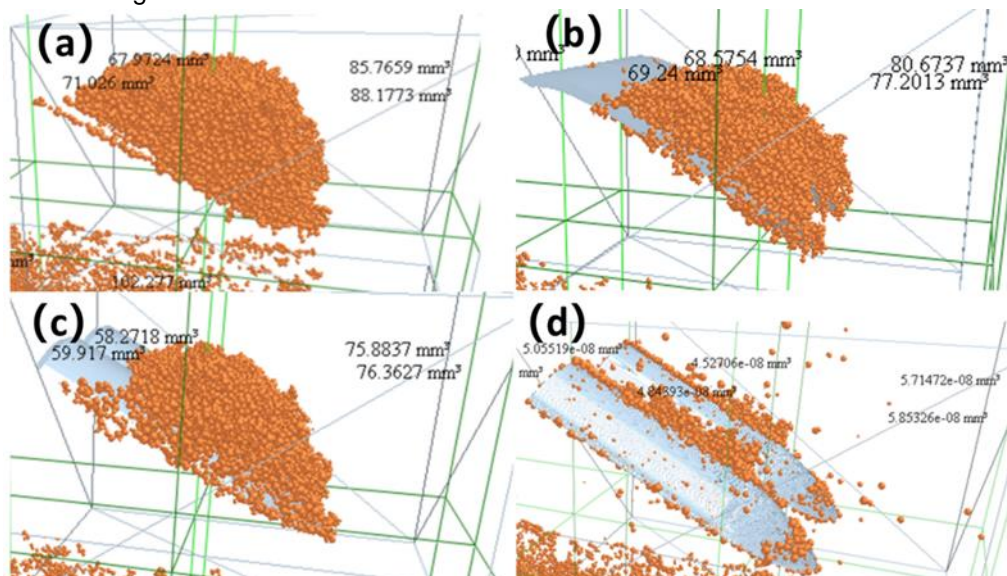

Fig. 16 - Soil adhesion to the surfaces of different types of shovels
(a) Conventional flat-plate harvester; (b) Bionic radian shovel; (c) Bionic smooth-surface shovel; (d) Bionic non-smooth-surface shovel

The bidirectional surface shovel, combined with the texture characteristics of the surface ridges (QL), has a significant effect. After the work stops, the soil volume attached to the shovel body is only 20.93897 E-08 mm^3, indicating that the non-smooth surface has a substantial impact on soil removal. Fig. 17 is a comparison of the pressures of four excavating shovels.
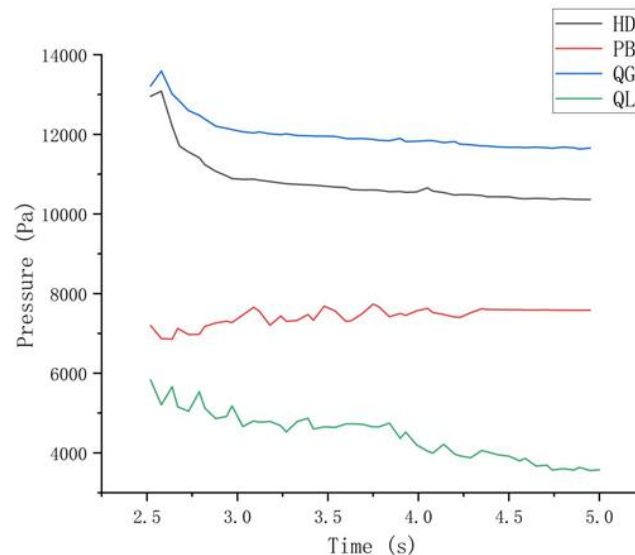
Fig. 17 - Contrast diagram of four kinds of excavating spades subjected to pressure

CONCLUSIONS

In this study, a potato-harvesting shovel based on the texture characteristics of pangolin scales was designed considering the unique external surface profiles of organisms, combined with knowledge of bionics, reverse engineering, soil adhesion mechanics, materials science, and other fields. Soil was collected during the potato-harvesting period and measured on the spot, and the soil groove model was established in stages after calibrating the soil particles parameters. The accuracy and scientific nature of the model were verified by comparing the soil on the surface of the excavating shovel after bionic and conventional shovelling.

(1) Compared with the existing potato-harvesting shovel design methods, the design method proposed in this paper has the following advantages.

Based on the natural behaviour and living environment of the pangolin, pangolin scales were found to be extremely similar to potato-harvesting shovels, providing the best harvest in certain respects. Therefore, according to the depth-of-field microscope observation results to search for a non-smooth ribbed surface with the best arrangement, combined with the discrete element method, the 0.5 mm diameter clearance arrangement was confirmed to be the optimal solution. In addition, the overall profile of the spade face was determined according to reverse fitting, and the mathematical model of the corresponding function was established. Simultaneously, various control groups were established and applied in the subsequent simulation tests.

(2) In calibrating the soil model parameters, it can be concluded from the factorial experiment that the soil accumulation angle is mainly dependent on the surface energy density and rolling friction. The smaller the total particle weight, the larger the surface area and surface energy. Therefore, it is impossible to solve the soil adhesion problem effectively from the perspective of broken soil. Therefore, from the angle of the surface energy, the continuity of water film on the surface is destroyed by making the surface non-smooth. Defining a reasonable calculation domain in the EDEM granular bed calculation could reduce the calculation time without affecting the whole.

(3) This design method can be applied to the design of other soil-touching parts of agricultural machinery, such as deep turning machines, deep loosening machines, and ditch openers. This approach is not limited to potatoes and has strong generality to solve the problem of soil desorption.

This design method can be applied to the design of other soil touching parts of agricultural machinery, such as deep turning machine, deep loosening machine, ditch opener, etc. Crops are not limited to potatoes, and have a strong generality to solve the problem of soil desorption. In order to make better use of bionics to solve the problem of soil adhesion of agricultural machinery, a database matching a variety of soil organisms with the actual production conditions of more agricultural machinery will be established in the future, so as to provide more inspirations for the design of agricultural machinery from the perspective of biology. This method ignores the fibre root agglomeration model of crops because only soil adhesion to the surfaces of shovels was analysed in this study. Therefore, to make our model closer to the actual soil environment, the next steps will be to add the characteristic parameters of the soil swelling force caused by roots and to perform further exploration by coupling the ANSYS and EDEM methods.

REFERENCES

[1]   Arnell, R. D. (2007). Two-body abrasive wear of the surfaces of pangolin scales. *J. Bionics Eng.,* 2, 77–84. DOI: 10.1016/S1672-6529(07)60017-1

[2]   Babbitt, D.M. (2008). Seed potato treatment on a large scale. *Am. Potato J.,* 8(12*)*, pp.271-272. DOI: 10.1007/BF02878789

[3]   Baran, O., Degennaro, A., Ramé, E., Wilkinson, A., Nakagawa, M., & Luding, S. (2009). DEM simulation of a Schulze ring shear tester. *Paper presented at the Int. Conf. Micromechanics of Granular Media.*

[4]   Celik, H. K., Cinar, R., Yilmaz, D., Ulmeanu, M. E., Rennie, A. E. W., & Akinci, I. (2019). Mechanical collision simulation of potato tubers. *J. Food Process Eng.,* 42(5), pp.e13078. DOI: ARTN e1307810.1111/jfpe.13078

[5]   Fisher, R. A. (1928). Further note on the capillary forces in an ideal soil. *J. Agric. Sci.,* 18(3). DOI: 10.1017/S0021859600019432

[6]   Greiner, C., & Schäfer, M. (2015). Bio-inspired scale-like surface textures and their tribological properties. *Bioinspir. Biomim., 10(4).* DOI: 10.1088/1748-3190/10/4/044001

[7]   Hao, F., Florent, L., Cihui, P., & Hui, H. (2021). Floorplan generation from 3D point clouds: A space partitioning approach. ISPRS J. Photogramm. *Remote Sens.*, 175, pp.44-55. DOI: 10.1016/j.isprsjprs.2021.02.012

[8]   Heath, M. E., & Hammel, H. T. (1986). Body temperature and rate of O_2 consumption in Chinese pangolins. *Am. J. Physiol.,* 250(3 Pt 2). DOI: 10.1152/ajpregu.1986.250.3.R377

[9]   Hou, Q., Yang, X., Cheng, J., Wang, S., Duan, D., Xiao, J., & Li, W. (2020). Optimization of performance parameters and mechanism of bionic texture on friction surface. *Coatings, 10(2).* DOI: 10.3390/coatings10020171

[10]   Hu, S. X. (2015). Study on parametric reverse modeling. *Appl. Mech. Mater.*, 3748.

[11]   Hunt, R. E. (1984). *Geotechnical engineering investigation manual: Geotechnical engineering investigation manual.* McGraw-Hill Book Company

[12]   Jafar, M., Mohsen, R. F., & Hassan, A. (2021). An optimized bionic electro-osmotic soil-engaging implement for soil adhesion reduction. *J. Terramechanics,* 95, pp.1-6. DOI: 10.1016/j.jterra.2021.01.003

[13]   Junior, R. A. A., Cheng, L.-Y., & Osello, P. H. S. (2019). An improvement of rigid bodies contact for particle-based non-smooth walls modeling. *Comp. Part. Mech.,* 6(4), pp.561-580. DOI: 10.1007/s40571-019-00233-4

[14]   Lee, K. H., Woo, H., & Suk, T. (2001). Point data reduction using 3D grids. *Int. J. Adv. Manuf. Tech., 18(3),* pp.201-210. DOI: 10.1007/s001700170075

[15]   Liu, S., Wang, Y., Jiang, H., Wei, Q., & Xiao, J. (2016). Aerial survey and scanning point cloud data acquisition & modeling technology for hydropower engineering. *5th Int. Conf. Advanced Materials and Computer Science*, 114-119.

[16]   Massah, J., Roubeneh, F.H., Roubeneh, Z. H., &Vakilian, K. A. (2020). Experimental investigation of bionic soil-engaging blades for soil adhesion reduction by simulating Armadillidium vulgare body surface. *INMATEH-Agricultural Engineering*, 60(1), pp. 99-106. DOI:10.35633/inmateh-60-11

[17]   Ren, L. Q., Tong, J., Li, J. Q., & Chen, B. C. (2001). SW—Soil and water: Soil adhesion and biomimetics of soil-engaging components: A review. *J. Agric. Eng. Res.,* 79(3), 239-263.
        DOI: 10.1006/jaer.2001.0722

[18]   ****Testing of physical properties of granular materials - Part 3: Measurement of fluidity index*, GB/T 31057.3-2018 C.F.R. (2018).

[19]   ****Testing of physical properties of granular materials - Part 2: Measurement of vibrational density*, GB/T 31057.2-2018 C.F.R. (2018).

[20]   Tong, J., Ma, Y.-H., Ren, L.-Q., & Li, J.-Q. (2000). Tribological characteristics of pangolin scales in dry sliding. *J. Mater. Sci. Letters,* 19(7), pp.569-572. DOI: 10.1023/A:1006769926391

[21] Tong, J., Zhang, Q., Guo, L., Chang, Y., Guo, Y., Zhu, F., Chen, D., Liu, X. (2015). Compaction performance of biomimetic press roller to soil. *J. Bionic Eng.,* 12(1), pp.152-159. DOI: 10.1016/S1672-6529(14)60109-8

[22] Wang, W., Song, J., Zhou, G., Pan, B., Wang Q., & Chen, L. (2022). Simulations and experiments of the seedbed straw and soil disturbance as affected by the strip-tillage of row cleaner (DEM). *INMATEH-Agricultural Engineering*, 66(1), pp:49-61. DOI: https://doi.org/10.35633/inmateh-66-05

[23] Xu, P. F., Duan, S. Y., & Wang, F. (2020). Reverse modeling and topological optimization for lightweight design of automobile wheel hubs with hollow ribs. *Int. J. Comput. Methods*, 17(09). DOI: 10.1142/S0219876219500646

[24] Yutaka, A., & Hajime, Y. (1972). Study on the adhesion of soil (Part 2): Theoretical analysis on the mechanism of adhesive force at the saturated stage. *Japanese J. Soil Sci. Plant Nutr.,* 43(8).

[25] Zenkov, S. A., & Lkhanag, D. (2020). Use of repair-recovery compositions for reducing the adhesion of soils to working bodies of machines. *IOP Conf. Ser.: Mater. Sci. Eng., 971(5)*. DOI: 10.1088/1757-899X/971/5/052051

[26] Zhang, L., Ren, L., Tong, J., & Shi, Y. (2004). Study of soil-solid adhesion by grey system theory. *Prog. Nat. Sci., 14(2)*, 119-124.

[27] Zhou, G., Ma, S., Han, D., Luo, G., Liu, F., & Zhang, R. (2016). Trafficability of rigid wheel with bionic lug on sand by 3D DEM, *Proceedings of the 2nd international conference on advances in mechanical engineering and industrial informatics,* Vol. 73, pp. 1648-1651.